

Calibration of the Dual-Frequency Precipitation Radar Onboard the Global Precipitation Measurement Core Observatory

Takeshi Masaki¹, Toshio Iguchi², *Fellow, IEEE*, Kaya Kanemaru³, Kinji Furukawa, Naofumi Yoshida, Takuji Kubota⁴, *Member, IEEE*, and Riko Oki

Abstract—This article describes four-year calibration results of the dual-frequency precipitation radar (DPR) onboard the Global Precipitation Measurement (GPM) Core Observatory. The calibration method basically follows the method that was used to calibrate the precipitation radar (PR) onboard the Tropical Rainfall Measuring Mission (TRMM) satellite. However, both the hardware and data processing method for calibration are improved by taking advantage of the lessons learned from the PR's calibration. Since the response of the radar receivers was found to depend on the waveform, the active calibrator was improved in such a way that the external calibration can be performed with both continuous and pulse waves. The methods for evaluating the calibration data were also improved. Instead of assuming a Gaussian antenna pattern, the effective beamwidths were determined by assuming an antenna pattern created by the Taylor distribution that was used to design the antennas. The results of the calibration including these improvements provide the new precise parameters of DPR's calibration. The new parameters increased the Ku-band precipitation radar's (KuPR's) radar reflectivity factor (Z) by about 1.3 dB and that of the Ka-band precipitation radar (KaPR) by about 1.2 dB from the precalibrated Z values, and the minimum detectable radar reflectivities were 15.46, 19.18, and 13.71 dBZ for KuPR, matched beam of KaPR, and high-sensitivity beam of KaPR, respectively. After applying the new calibration methods to both DPR and PR, normalized radar cross sections (σ^0) from the DPR and PR agree with each other.

Index Terms—Calibration, Global Precipitation Measurement (GPM), spaceborne precipitation radar (PR), Tropical Rainfall Measuring Mission (TRMM).

NOMENCLATURE

ARC Active radar calibrator.
BPF Bandpass filter.

Manuscript received February 21, 2020; revised August 12, 2020 and October 23, 2020; accepted November 6, 2020. Date of publication December 14, 2020; date of current version December 2, 2021. This research was funded by Japan Aerospace Exploration Agency, Tsukuba, Japan. (*Corresponding author: Takeshi Masaki.*)

Takeshi Masaki is with the Remote Sensing Technology Center of Japan, Tsukuba 305-8505, Japan (e-mail: masaki_takeshi@restec.or.jp).

Toshio Iguchi is with the Earth System Science Interdisciplinary Center, University of Maryland, College Park, MD 20742 USA.

Kaya Kanemaru is with the National Institute of Information and Communications Technology, Koganei 184-8795, Japan.

Kinji Furukawa is with the Satellite Applications and Operations Center, Japan Aerospace Exploration Agency, Tsukuba 305-8505, Japan.

Naofumi Yoshida is with the Remote Sensing Technology Center of Japan, Tokyo 105-0001, Japan.

Takuji Kubota and Riko Oki are with the Earth Observation Research Center, Japan Aerospace Exploration Agency, Tsukuba 305-8505, Japan.

Digital Object Identifier 10.1109/TGRS.2020.3039978

CW Continuous wave.
DPR Dual-frequency precipitation radar.
FCIF Frequency converter and intermediate frequency.
FEPT Final electrical performance test.
GMI GPM microwave imager.
GPM Global Precipitation Measurement.
JAXA Japan Aerospace Exploration Agency.
KuPR Ku-band precipitation radar.
KaPR Ka-band precipitation radar.
LoAmp Logarithmic amplifier.
LUT Lookup table.
NASA National Aeronautics and Space Administration.
NICT National Institute of Information and Communications Technology.
PR Precipitation radar.
PRF Pulse repetition frequency.
Rx Receiver.
SCDP System control data processing.
SSPA Solid state power amplifier.
TRMM Tropical Rainfall Measuring Mission.
TRS Transmitter and receiver system.
Tx Transmitter.

I. INTRODUCTION

THE GPM mission is an international satellite mission led by NASA of the United States and JAXA of Japan to unify and advance precipitation measurement [1]. The mission contributes not only to meteorological studies but also to studies of climate water cycle change, flood prediction, numerical weather forecast, and many other applications through observing the global precipitation with the GPM Core Observatory and several constellation satellites [2]. The GPM Core Observatory, which carries the DPR [3]–[7] and the GMI [8]–[10], was jointly developed by NASA and JAXA and launched in February 2014 from Japan. Simultaneous observations of precipitation by the DPR which provides 3-D structure of precipitation and by the GMI which measures microwave emission from rain and scattering by snow create a reliable database that is used by other constellation satellites to estimate precipitation rate [11]–[13]. In other words, the accuracy of the precipitation estimates by the DPR and GMI is critical to the success of the GPM mission.

The DPR, which consists of the KuPR and the KaPR, was jointly developed by JAXA and NICT. The mission requires that the DPR be calibrated within ± 1 dB because the estimation of precipitation rate depends significantly on the calibration. If the calibration error exceeds 1 dB, for example, more than 10% of estimation error in precipitation rate may result. Although the characteristics of the components of the DPR were carefully measured in ground tests before launch, it is necessary to calibrate the DPR onboard after launch because the characteristics of some components and the overall performance may have changed during and after launch. This article describes the calibration of the DPR that was carried out after launch.

The PR, whose design and operating frequency was almost identical to the KuPR, onboard the TRMM satellite [14]–[16] had been calibrated until its mission completed in April 2015. The PR is calibrated by a method that combines two kinds of calibration as reported by Takahashi *et al.* [17] (hereafter T03): one is the internal calibration and the other one is the external calibration. The internal calibration is carried out to check the performance of the radar's Rx system, especially the relationship between the received power and the recorded digital count which is the Rx's analog-to-digital converter's digital output. The external calibration is carried out to check not only the Rx system but also the whole radar system including the radar's antenna and Tx system by using a ground-based calibrator that works in coordination with the spaceborne radar. We call this calibration instrument the ARC hereafter. The calibration of the DPR basically follows the calibration method described in T03, but we have introduced some improvements such as a new improved calibrator and a calibration method taking advantage of the lessons learned from the PR's calibration. The new calibration parameters employed the standard DPR level-1 products in version 5 (V5) released in May 2017.

This article describes the improved calibration method with the new calibrator and the results of four-year onboard calibration of the DPR. Outline of the calibration is described in Section II. Descriptions of the new calibrator are explained in Section III. The method of calibration and configurations are described in Sections IV and V, respectively. The results of calibration are represented in Section VI and summarized in Section VII.

II. OUTLINE OF THE CALIBRATION

The calibration for the DPR is conducted to correctly derive the radar reflectivity from the precipitation echoes. When the antenna pattern is a Gaussian and the transmitted pulse is a rectangle pulse, the measured radar reflectivity factor without any attenuation corrections (Z_m in mm^6/m^3) is expressed as follows [18]:

$$Z_m = \frac{2^{10} \cdot 10^{18} \cdot \ln(2)}{\pi^3 c} \cdot \frac{\lambda^2 r^2 P_r}{G_t G_r \theta_a \theta_c \tau |K|^2 P_t} \quad (1)$$

where c is the light speed in a vacuum, λ is the wavelength of the radar, r is the distance from radar to targets, G_t is the Tx antenna gain of the radar, G_r is the Rx antenna gain of the radar, θ_a is the -6 dB width of the two-way Gaussian antenna

pattern in the along-track direction, θ_c is the -6 dB width of the two-way Gaussian antenna pattern in the cross-track direction, τ is the pulsewidth of the rectangular transmitted pulse, K^2 is the dielectric factor, P_t is the transmitted peak power of the radar's pulse wave, and P_r is the received power of the radar. Since the DPR can measure only P_r which is composed of signals from volume targets such as precipitation and background noise, the background noise is required to be removed in the estimation of precipitation. In the case of the external calibration, however, the background noise is negligible because the magnitude of ARC's signal power is sufficiently greater than that of background noise. Note that P_t and P_r are defined as the powers at the antenna feed point located between the DPR antenna and the TRS [3].

The main purpose of the radar's calibration is to determine the magnitude of the parameters that appear in (1). In particular, determination of the parameters after launch is important because some of them may have changed after launch due to the environmental changes even though the parameters were measured carefully in the FEPT on ground before launch. Some of the parameters are well-defined constants or expected to be stable. For instance, λ is determined by a very stable crystal oscillator, and r is also accurately determined by the echo delay. It is not possible to calibrate each parameter in (1) separately after launch. As explained below, we determine $P_t G_t$ and P_r / G_r by using an ARC. θ_a and θ_c are estimated by examining the angle dependence of the DPR's Rx power measured by the ARC and the ARC's Tx measured by the DPR. Therefore, (1) can be simply expressed as a function of a few critical parameters that determine the radar calibration

$$Z_m = f(\lambda, |K|^2, P_t G_t, P_r / G_r, \theta_a, \theta_c, \tau). \quad (2)$$

$|K|^2$ in (1) is set to 0.9255 for Ku-band and 0.8989 for Ka-band by using the permittivity of water at 10°C [19]. For τ , we evaluated DPR's pulse waveforms measured by the ARC after launch and by the sea surface echo at the nadir incidence [20]; as a result, we consequently adopted the parameters obtained from the FEPT.

We can determine the magnitudes of $P_t G_t$ and P_r / G_r by measuring the power of the transmitted/received electromagnetic signals between the spaceborne radar (PR or DPR) and the ARC. Here, $P_t G_t$ is the equivalent isotropic radiated power (EIRP) in front of the DPR antenna and P_r / G_r is the radar input power (S_a) in front of it. Fig. 1 outlines the calibration for the DPR with the ARC. The magnitudes of EIRP and S_a for the radar are calibrated by comparing these quantities (EIRP and S_a) with those of the ARC. In particular, for the DPR as Tx and ARC as Rx we use (3) and for the DPR as Rx and ARC as Tx we use (4) where

$$\begin{aligned} \text{EIRP(RADAR)}[\text{dBm}] &= \text{EIRP(RADAR}_0\text{)}[\text{dBm}] + \delta\text{EIRP}[\text{dB}] \\ &= \text{EIRP(ARC)}[\text{dBm}] \end{aligned} \quad (3)$$

$$\begin{aligned} S_a(\text{RADAR})[\text{dBm}] &= S_a(\text{RADAR}_0) + \delta S_a[\text{dB}] \\ &= S_a(\text{ARC})[\text{dBm}]. \end{aligned} \quad (4)$$

Here, the $\text{EIRP(RADAR}_0\text{)}$ is the EIRP obtained from the FEPT, δEIRP is the calibration correction for the DPR Tx

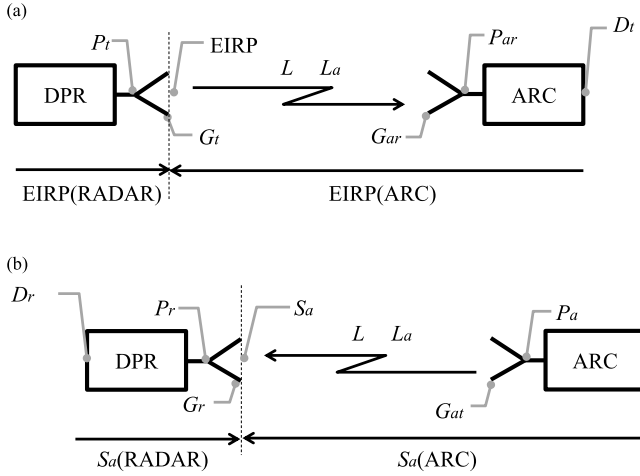


Fig. 1. Schematic images of evaluation process for DPR's Tx and Rx systems. (a) DPR Tx system. P_t is the DPR's transmitted power. G_t is the DPR Tx antenna gain. EIRP is the equivalent isotropic radiated power. L is the free-space propagation loss. L_a is the one-way atmospheric attenuation loss. G_{ar} is the ARC Rx antenna gain. P_{ar} is the input power at the feed point of ARC Rx antenna. D_t is the digital count recorded by ARC. (b) DPR Rx system. D_r is the digital count recorded by DPR. P_r is the DPR's received power. G_r is the DPR Rx antenna gain. S_a is the radar input power in front of DPR antenna. G_{at} is the ARC Tx antenna gain. P_a is the ARC's transmitted power at the feed point of ARC Tx antenna.

system, $S_a(\text{RADAR}_0)$ is the S_a obtained from the FEPT, and δS_a is the calibration correction for the DPR Rx system. EIRP(ARC) and $S_a(\text{ARC})$ are calculated as follows:

$$\text{EIRP(ARC)}[\text{dBm}] = P_{ar}[\text{dBm}] - G_{ar}[\text{dB}] - L_a[\text{dB}] - L[\text{dB}] \quad (5)$$

and

$$S_a(\text{ARC})[\text{dBm}] = P_a[\text{dBm}] + G_{at}[\text{dB}] + L_a[\text{dB}] + L[\text{dB}] \quad (6)$$

where P_{ar} is the input power at the feed point of the ARC Rx antenna, G_{ar} is the ARC Rx antenna gain, L_a is the one-way atmospheric attenuation loss, L is a free space propagation loss, P_a is the ARC's transmitted power at the feed point of the ARC Tx antenna, and G_{at} is the ARC Tx antenna gain. L and L_a are

$$L = 20 \log_{10} \left(\frac{\lambda}{4\pi r_t} \right) [\text{dB}] \quad (7)$$

$$L_a = - \int_0^{r_t} (k_{\text{oxy}} + k_{\text{wv}} + k_{\text{cld}}) ds [\text{dB}] \quad (8)$$

where r_t is the range distance between DPR and ARC, k_{oxy} is the attenuation caused by molecular oxygen, k_{wv} is the attenuation due to water vapor, and k_{cld} is the attenuation by cloud liquid water. Thus, the calibration for the DPR with the ARC requires the parameters used in (3)–(8). To conduct the calibration, functions of the ARC (in Section III) and methods of the calibration (in Section IV) are introduced.

III. DESCRIPTION OF THE ARC

In the external calibration of the DPR, the DPR operational mode is changed from the normal observation mode to a mode dedicated for the external calibration. The scan pattern and the

range sampling window are changed in the external calibration mode with the other parameters unchanged. The overlapping beam pattern enables the ARC to be located within multiples of radar beams so that the antenna gain at various directions within the main beam can be measured (details are described in Section IV-C). The external calibrations are performed only at near nadir angles and its range sampling window is set to about -25 km relative to the surface when the ARC's elevation-angle is maximum. External calibration data are collected during a prescheduled satellite overpass by using two new ARCs called KuARC and KaARC (hereinafter both are collectively called DPR-ARC) which are developed to calibrate KuPR and KaPR, respectively. Thus, the data obtained by the DPR and DPR-ARC during external calibration are analyzed using the procedure described in Section IV.

Table I lists the specifications of the DPR-ARC. Basic functions of the ARC are similar to the ARC for the TRMM PR (PR-ARC), which receives the radar's Tx pulse waves and transmits a signal to the radar. The antenna gains of the DPR-ARC and PR-ARC were accurately calibrated against a national standard at NICT. The DPR-ARC has three operational modes as listed in Table II. The "Rx mode" is the mode only for receiving DPR's Tx pulse signals, which is not used in normal external calibration, "CW calibration" is the mode for the external calibration with CWs from the ARC, and "pulse calibration" is the mode for the calibration with pulse waves from the ARC. The DPR-ARC's Tx and Rx systems are independent so that they can simultaneously calibrate for DPR's Tx and Rx systems at the timing of a satellite overpass event by using the CW and pulse calibration. Note that it is also possible to use the received signal as a trigger for changing the transmission timing and duration from the ARC. As for the PR-ARC, although the "transponder mode" [17] could calibrate the PR's Tx and Rx systems simultaneously, it differs from the DPR-ARC's CW and pulse calibration in that the PR-ARC does not transmit a signal generated by ARC itself to the radar. Each operational mode of the DPR-ARC and PR-ARC is set for one external calibration.

Fig. 2 shows a block diagram of the KuARC's and KaARC's Tx system for calibrating the DPR Rx system. Both the DPR and PR transmit and receive two slightly different frequencies called f_1 and f_2 nearly simultaneously [3], [16]. This is a technique called "frequency agility" to increase the number of independent samples and thereby reducing the sampling error of the received signal [16]. Therefore, it is desirable that the ARC can transmit signals of both frequencies nearly simultaneously. In the case of the DPR-ARC, signals of two frequencies are generated by the phase-locked oscillators and go through the switches which can select pulse wave or CW. Then, the signals combined by a combiner go through the several components and are finally transmitted toward the DPR through Route 1 of Fig. 2. The transmitted power at the antenna feed can be measured by an external instrument of well-calibrated power meter through Route 2 of Fig. 2 after the satellite overpass.

The Rx response of both DPR and PR depends on the waveform and a pulse input is preferable to a CW input as it better represents the measurement of interest (details

TABLE I
SPECIFICATIONS OF KUARC AND KAARC. ANTENNA GAINS OF BOTH DPR-ARC AND PR-ARC WERE REMEASURED BY NICT

Item1	Item2	KuARC	KaARC	PR-ARC	
Rx	Center frequency	13.597GHz(f1) for KuPR	35.547GHz(f1)	13.796GHz(f1)	
		13.603GHz(f2) for KuPR	35.553GHz(f2)	13.802GHz(f2)	
		13.796GHz(f1) for PR			
		13.802GHz(f2) for PR			
	Sampling resolution	0.1 μ s	0.1 μ s	1080 μ s (peak hold)	
	Waveform	Pulse	Pulse	Pulse	
	Antenna gain	19.87 dBi	20.77 dBi	23.65 dBi	
	Dynamic range	48 dB	48 dB	50 dB	
	Accuracy	\pm 0.5 dB	\pm 0.5 dB	\pm 0.5 dB	
Tx	Center frequency	13.597GHz(f1) for KuPR	35.547GHz(f1)	13.796GHz(f1)	
		13.603GHz(f2) for KuPR	35.553GHz(f2)	13.802GHz(f2)	
		13.796GHz(f1) for PR			
		13.802GHz(f2) for PR			
		Waveform	CW or Pulse	CW or Pulse	CW
		Number of pulse wave	Variable	Variable	Fix
		PRF	Variable	Variable	Fix
		Delay	Variable	Variable	30 μ s
		Pulsewidth	1.6 μ s	1.6 μ s or 3.2 μ s	1.67 μ s
		Maximum Tx power	28.5 dBm	29.2 dBm	28.6 dBm
		Antenna gain	19.87 dBi	20.64 dBi	23.73 dBi
		Accuracy	\pm 0.5 dB	\pm 0.5 dB	\pm 0.5 dB
		Beamwidth	17.3° (H-plane)	17.0° (H-plane)	10.7° (H-plane)
			15.4° (E-plane)	14.4° (E-plane)	10.3° (E-plane)

TABLE II
COMPARISON OF OPERATIONAL MODE BETWEEN
DPR-ARC AND PR-ARC

ARC	Mode name	Rx	Tx
PR-ARC	Rx mode	✓	—
	Tx mode	—	CW
	Transponder mode	✓	Pulse (Radar's Tx pulse)
DPR-ARC	Rx mode	✓	—
	CW calibration	✓	CW
	Pulse calibration	✓	Pulse

are described in Section IV-B), that is, pulse calibration of DPR-ARC and transponder mode of PR-ARC are preferred to use. A new function of the DPR-ARC's Tx system to transmit pulse waves with a higher PRF than the DPR's PRF is introduced. This function enables the DPR to measure accurately the peak power of the ARC's Tx pulse signals. In general, a radar samples the received signals at a timing of the predetermined sampling interval (i.e., range-bin). The ARC's Tx pulse signals are not necessarily received at the center of the range-bin. For the DPR, the received pulse shape is deformed by passing through the radar's BPF so that the power sampled off-center of the sample range-bin is lower than the peak power of the received pulse shape. As a result, the intensity of the actual signals depends on the sample time that determines the relative deviation from the center of range-bin. In the case of the calibration for the TRMM PR with the transponder mode, the PR transmits 32 pulse waves in a beam and the PR-ARC returns each pulse with a constant delay to

the PR so that the returned signal power measured by the PR varied with the distance between PR and ARC and was slightly underestimated because the returned pulse was not necessarily sampled at its peak. In fact, T03 showed a large fluctuation of the returned power when the PR was calibrated in the transponder mode. On the other hand, the DPR-ARC transmits a series of pulses of a known power at the PRF of 288 kHz which is much higher than the DPR's PRF of about 4 kHz. Since the DPR-ARC's Tx pulse waves are received by the DPR's range-gate sampling interval of 250 m during the external calibration, several pulses are sampled in each beam. Because there are about 100 sampling range-bins in each beam when the ARC's elevation-angle is maximum, and their frequency does not synchronize with the ARC's PRF, the peak power of the DPR-ARC's Tx pulse signals can be measured accurately from the envelope of the sampled powers.

Since the DPR-ARC can transmit pulse waves by ARC itself, a method for measuring the intensity of ARC's Tx pulse waves is also improved. In the case of the transponder mode of calibration with the PR-ARC, the transmitted power from the ARC had to be calculated by using the ARC's loop-gain that was determined with a CW using an external source of signal generator because the PR-ARC was not able to generate pulse waves. T03 mentioned that the fluctuation of the loop-gain was one of the possible causes of the large calibration error in the transponder mode. On the other hand, since the DPR-ARC can transmit pulse waves by ARC itself, the transmitted power can be calibrated directly with an external instrument of power meter (i.e., Route 2 of Fig. 2). This improvement reduces the calibration error.

Fig. 3 shows a block diagram of the KuARC's and KaARC's Rx system for calibrating the DPR Tx system. Signals received

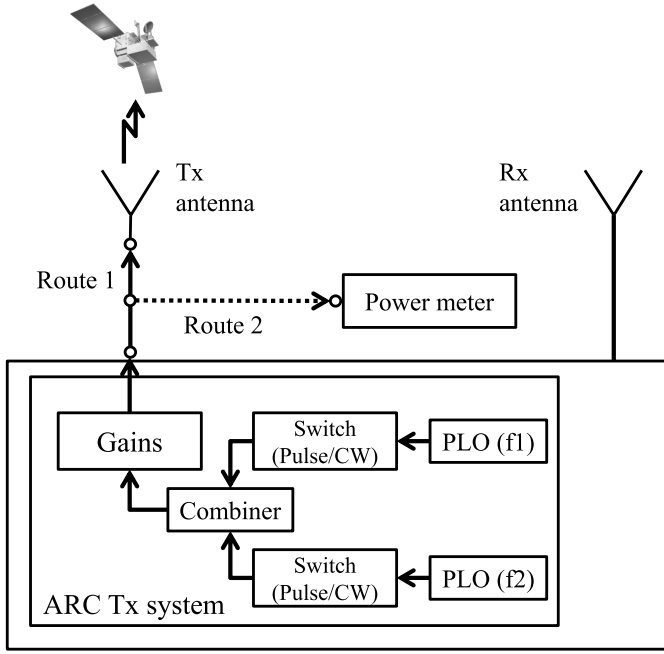


Fig. 2. Block diagram of KuARC's and KaARC's Tx systems. Both have the same configuration but are independent systems. CW is continuous wave. PLO is a phase-locked oscillator.

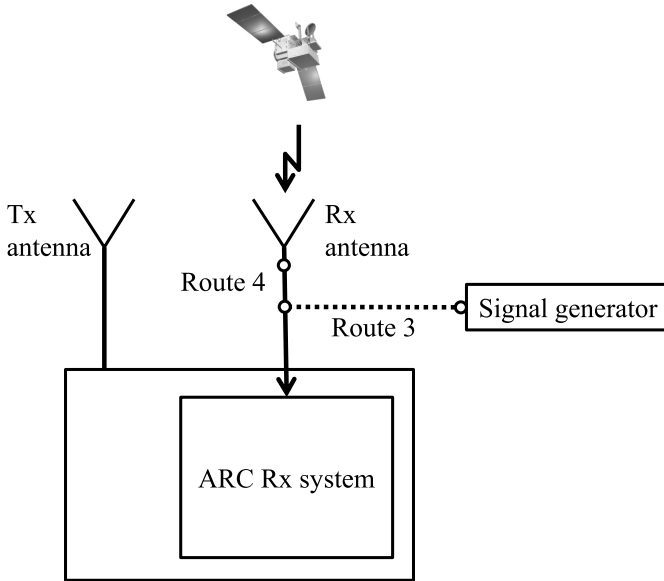


Fig. 3. Block diagram of KuARC's and KaARC's Rx systems. Both have the same configuration but are independent systems.

by the DPR-ARC Rx antenna pass through several components and are finally recorded as digital counts.

One of the new functions of the DPR-ARC Rx system is to record the signals with a sampling resolution higher than that of the PR-ARC. The sampling resolution is $0.1 \mu\text{s}$ which is approximately 10^4 times finer than the PR-ARC. This improvement enables the DPR-ARC to capture the overall waveform clearly while the PR-ARC was able to detect only the peak of received signal with a peak hold circuit.

The DPR and PR transmit pulsed waveforms of frequencies f_1 and f_2 nearly simultaneously. However, the design of the ARC allows reception of the signal at only a single frequency. Therefore, we assume that the intensity of transmitted power at f_1 is the same as that at f_2 in the calibration because the Tx's in the DPR are operated in a saturated state and since f_1 and f_2 are essentially identical. In fact, they were measured to be effectively the same in the FEPT.

IV. METHOD OF THE CALIBRATION

A. Calculation of $EIRP(ARC)$ and $S_a(ARC)$

As described in Section II, several parameters are examined to calculate $EIRP(ARC)$ and $S_a(ARC)$. L is given from λ and r_t , and computation of L_a requires estimation of a one-way atmospheric attenuation loss. T03 used a constant value of the atmospheric attenuation loss for all PR's external calibrations. For DPR, however, the magnitude and uncertainty of the atmospheric attenuation loss at Ka-band are larger than those at Ku-band. Therefore, we use an instantaneous estimate of the atmospheric attenuation loss provided by the corresponding standard DPR level-2 products which contain a two-way total atmospheric attenuation loss (named "piaNP") by integrating k_{oxy} , k_{wv} , and k_{cld} based on the Global Objective Analysis Data [18].

To estimate $EIRP(ARC)$, we convert a digital count (D_t) recorded by the DPR-ARC to P_{ar} in (5) by the LUT that is made by calibrating the DPR-ARC itself. In the calibration, an external, well-calibrated signal generator is connected to the ARC's Rx system with a coaxial cable as shown in Route 3 of Fig. 3. Then, pulse waves whose waveform and PRF are almost the same as those of the DPR Tx pulse waves are fed to the ARC. The output power of signal generator (P_{SG}) is controlled in 1-dB steps by the software of the ARC, and the signal is recorded as a digital count (D_{SG}). Finally, the LUT is constructed by optimizing the relationship between P_{SG} and D_{SG} by linearly interpolating the intervals. The LUT should be updated on each external calibration because the DPR-ARC Rx system depends on temperature which can lead to variations in the gain of the DPR-ARC of approximately ± 0.5 dB. After the ARC calibration itself, we connect the coaxial cable to the DPR-ARC Rx antenna as shown in Route 4 of Fig. 3. During the external calibration, the DPR transmits the same number of pulses at f_1 and f_2 for a total of about 100 pulses in one beam. All of them can be received by the ARC, and their recorded peaks at f_1 are averaged for evaluating the DPR Tx system. To estimate $S_a(ARC)$, P_a is measured with a power meter as described in Section III.

B. Calculation of $EIRP(RADAR_0)$ and $S_a(RADAR_0)$

$EIRP(RADAR_0)$ is related to other parameters as follows:

$$EIRP(RADAR_0)[\text{dBm}] = P_{t0}[\text{dBm}] + G_{t0}[\text{dB}] \quad (9)$$

$$P_{t0}[\text{dBm}] = \sum_{i=1}^{128} P_{s0}(i)[\text{dBm}] + C_{t0}[\text{dB}] \quad (10)$$

where P_{t0} is the DPR's transmitted power estimated with the parameters at the FEPT, G_{t0} is the DPR Tx antenna gain

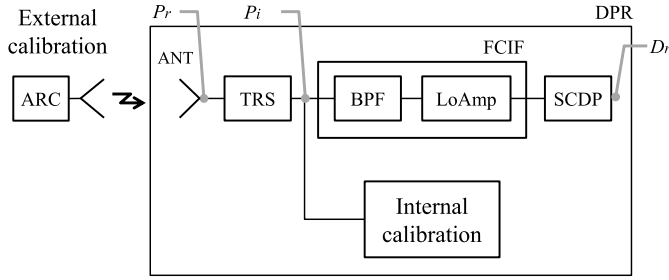


Fig. 4. Schematic of the external calibration and the internal calibration. ANT is antenna. TRS is transmitter and receiver system. BPF is bandpass filter. LoAmp is logarithmic amplifier. SCDP is system control data processing.

measured at the FEPT, $P_{s0}(i)$ is the power of the i th SSPA the total of which makes the whole Tx amplifier measured at the FEPT, and C_{r0} is a correction value for the DPR Tx system at the FEPT (initially $C_{r0} = 0$). Since the SSPAs have temperature characteristics, we need to compensate for them by linearly interpolating the database with the actual temperature measured onboard. The database was made by the results obtained under controlled temperature environments on the ground before launch.

In addition, we define the $S_a(\text{RADAR}_0)$ as follows in logarithmic scale:

$$S_a(\text{RADAR}_0)[\text{dBm}] = P_{r0}[\text{dBm}] - G_{r0}[\text{dB}] \quad (11)$$

where P_{r0} is the DPR's received power and G_{r0} is the DPR Rx antenna gain measured at the FEPT. The P_{r0} is given in logarithmic scale as follows:

$$P_{r0}[\text{dBm}] = P_{i0}[\text{dBm}] - G_{\text{RS}0}[\text{dB}] - C_{r0}[\text{dB}] \quad (12)$$

$$P_{i0}[\text{dBm}] = \text{FCIF_LUT}_0(D_r) \quad (13)$$

where P_{i0} is the input power of the FCIF estimated with the parameters at the FEPT, $G_{\text{RS}0}$ is the gain of TRS G_{RS} measured at the FEPT (see Fig. 4), C_{r0} is a correction value for the DPR Rx system at the FEPT (initially $C_{r0} = 0$), FCIF_LUT_0 is the LUT of FCIF obtained at the FEPT, and D_r is the digital count recorded by the SCDP. Note that τ and a total gain of the DPR Rx system (G_{RS}) also have temperature characteristics and are compensated as well.

Fig. 4 illustrates a schematic of the external calibration and the internal calibration. During the external calibration mode, the signals transmitted by the ARC are received at the DPR antenna, and then, go through the TRS, BPF, and the LoAmp in the FCIF. Finally, the signals are recorded by SCDP as digital counts. The relationship between the input power P_i to the FCIF and the digital count D_r is derived from the FCIF_LUT which is obtained by the internal calibration. During the internal calibration mode, the pulse waves are generated by the crystal oscillator as input to the FCIF and go through the BPF and LoAmp, and are finally recorded by the SCDP. In the internal calibration loop, 32-step attenuators whose attenuation is 2.6 dB per step are automatically controlled so that the input–output characteristics of the FCIF over 80-dB dynamic range can be obtained. By averaging a large amount of internal calibration data, we can establish the FCIF_LUT

which produces the slope and the intercept of the relationship between P_i and D_r . P_r is provided by subtracting G_{RS} from P_i and its absolute magnitude is determined through the external calibration. Hence, the slope of the relationship between P_r and D_r is determined by the internal calibration and its intercept is effectively modified by the external calibration.

It turned out that the response of the DPR Rx system depends on the waveform (details are described in Appendix A). The gain of the Rx system for pulses differs slightly from that for CWs. As a result, we have to consider a different response of the DPR Rx system depending on the waveform. The relationship between the count value D_r and the input power P_i in the CW calibration and pulse calibration can be expressed as follows:

$$P_{ic} = A_c \cdot D_r + B_c \quad (14)$$

$$P_{ip} = A_p \cdot D_r + B_p \quad (15)$$

where P_{ic} is P_i for the CW calibration, A_c is the slope and B_c is the intercept of that the linear relationship between P_{ic} and D_r . P_{ip} , A_p , and B_p are similarly defined for the pulse calibration. A_p and B_p are provided by the internal calibration which uses pulse waves, however, A_c and B_c are not available from the internal calibration. Therefore, A_c and B_c were obtained using the results of BPF and LoAmp characteristics with CWs on the ground test.

C. Antenna Pattern Estimation

To calculate $\text{EIRP}(\text{RADAR}_0)$ and $S_a(\text{RADAR}_0)$ in (9) and (11), DPR's Tx and Rx powers must be measured at the center of the antenna pattern. Since the ARC is not generally located at the center of the DPR's beam, the peak power should be estimated with received power pattern of DPR and DPR-ARC. During normal observations, KuPR and KaPR scan a width of 245 and 125 km, respectively, with 49 beams per scan in the cross-track direction [3]. On the other hand, the center scan angle of the DPR is changed to direct the DPR's beam to the ARC during external calibration, and both of KuPR and KaPR's normal swaths are reduced to a 24-km swath with 49 beams per scan in the cross-track direction. Here, the 49 beams are divided into three subscans and one beam as shown in Fig. 5 so that the ARC is the center of the scan to evaluate the DPR's antenna pattern in detail. The first, second, and third subscans consist of the angle-bin number 2–17, 18–33, and 34–49, respectively. The remaining one beam (i.e., angle-bin number 1) is directed at the center of the narrowed swath. Thus, the sampling intervals are four times denser in the cross-track direction and about three times denser (only the scan angle at the center of the narrowed swath is four times denser) in the along-track direction compared to the normal observation. Such a change in the scan pattern is performed in ± 2.5 min as the DPR passes over the ARC.

During the external calibration mode, the DPR receives the DPR-ARC's Tx beam and the DPR-ARC receives the DPR's Tx beam while the DPR scans in the vicinity of the DPR-ARC. We assume that the antenna patterns of the DPR at different scan angles are the same after the correction of $\cos\theta$ dependence where θ is the angle from the normal to the

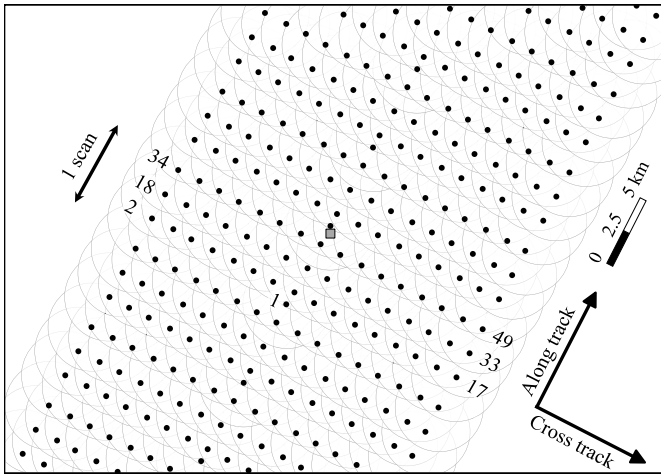


Fig. 5. Illustration of DPR's scan pattern during the external calibration mode. Circles indicate the beams of both KuPR and KaPR during the external calibration mode. Dots indicate the center of beams. Numbers attached to dots indicate the angle-bin number. The square indicates DPR-ARC's location.

antenna aperture. Since the KuARC's beamwidth of $\sim 15.4^\circ$ at E-plane $\sim 17.3^\circ$ at H-plane and the KaARC's beamwidth of $\sim 14.4^\circ$ at E-plane $\sim 17.0^\circ$ at H-plane are much wider than the DPR's beamwidth of $\sim 0.71^\circ$, the actual received powers by the DPR and the ARC are effectively determined only by the DPR Rx antenna pattern and the DPR Tx antenna pattern, respectively.

Even though the DPR measures signals at denser angle intervals in the external calibration mode than in the normal observation, the received power pattern with respect to the angle looks discrete (see Section VI-B). To obtain a precise peak power at the beam center, it is necessary to fit a model antenna pattern to the received power pattern. In this study, we adopted the Taylor distribution whose maximum sidelobe level in the DPR's design is -35 dB, and fit it to the actual data in linear scale by using the Levenberg–Marquart minimization method [22] to obtain the antenna pattern parameters. To calculate the relative angles, the scan angles of the DPR were used for the cross-track direction and the angles derived from satellite's position were used for the along-track direction.

The accuracy of fitting the actual data to the Taylor distribution affects the reliable estimation of the DPR's antenna pattern. In the case of the PR calibration, T03 used a parabolic curve fitting in logarithmic scale assuming that the PR's antenna pattern is approximated to the Gaussian distribution even though the hardware design of the PR was the Taylor distribution. It adopted 1-D fitting twice: the cross-track 1-D fitting was conducted after the along-track 1-D fitting. In the case of the DPR calibration, 2-D fitting is applied for the antenna pattern estimation in the along- and cross-track directions. Strictly speaking, the Gaussian distribution and the Taylor distribution are different. Fig. 6 shows one-way antenna patterns of the Taylor distribution and the Gaussian distribution in 1-D assuming -3 dB width of 0.71° . The differences between them become larger away from the center of the main lobe clearly. Here, we assume the interval of those distributions as the interval of DPR external calibration's scan pattern

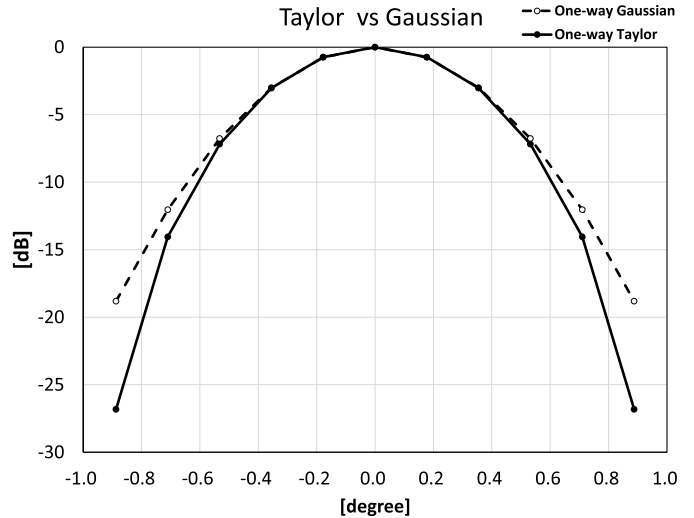


Fig. 6. One-way antenna patterns of the Taylor and the Gaussian distributions in 1-D assuming -3 dB width of 0.71° for both antennas. Points are plotted at intervals of 0.1775° . Solid and dashed lines indicate the Taylor distribution and dashed line indicates the Gaussian distribution, respectively. Horizontal axis denotes horizontal angle ($^\circ$) and vertical axis denotes power (dB).

(thus, the interval is 0.1775°) and fit the Gaussian distribution with Taylor distribution in logarithmic scale. If we use only the data which are located less than 3 dB below the peak (i.e., within $\pm 0.355^\circ$), the peak and beamwidth of the antenna pattern are, respectively, estimated to be 0.0 dB and 0.71° which are unaffected by the discrepancy between the Gaussian distribution and Taylor distribution. On the other hand, in the case of using the data which are located within 14 dB below the peak (i.e., within $\pm 0.710^\circ$), the peak and beamwidth become 0.3 dB and 0.66° , respectively, thus, the results differ from the original parameters of the Taylor distribution.

Even though the range of fitting needs to be narrowed to reduce this error, a limitation for the number of samples makes it difficult. For instance, in the case of the DPR, only ~ 10 data points for the fitting in 2-D are available within 3 dB below the peak power. Indeed, since the actual data observed by the external calibration includes some measurement errors, the estimation of the DPR's antenna pattern with a few data points may degrade the estimation accuracy. Taking account of the number of available data points and signal-to-noise ratios of DPR and ARC, we consequently adopted the fitting to Taylor distribution by using the data within 10 dB below the peak. When we use the data within 10 dB below the peak, ~ 30 data points are available for the fitting in 2-D.

This study also derives the appropriate beamwidth, which is the two-way Gaussian beamwidth used in (1), from the antenna pattern estimation with the Taylor distribution. This estimation gives the peak power, the beamwidths in the along- and cross-track directions, and the beam center position of the radar's one-way Taylor antenna pattern. If the radar's one-way antenna pattern is a Gaussian, the radar's two-way antenna pattern is also Gaussian, and its -6 dB width of the two-way antenna pattern can be simply obtained from the -3 dB width of the one-way antenna pattern. However, the sampling volume of the two-way Gaussian antenna pattern is slightly different from two-way Taylor antenna patterns.

TABLE III
IMPROVEMENTS OF THE DPR EXTERNAL CALIBRATION FROM THE PR CALIBRATION

Item1	Item2	Item3	DPR	PR
ARC	Tx pulse wave	PRF Source	Higher than radar ARC itself	Fixed PRF Radar (Transponder)
	Tx frequency		f1 and f2	f1 or f2
	Rx sampling		0.1 μ s	1080 μ s
Analysis	Fitting	Antenna pattern Fitting methods	Taylor	Gaussian
			2-D fitting in linear scale	1-D fitting in logarithmic scale

This study takes such discrepancy into account by introducing the effective beamwidth whose energy (volume integration of the power) of the product of one-way Taylor antenna patterns is the same as the ideal two-way Gaussian antenna pattern, that is,

$$\int_0^{2\pi} \int_0^\pi G_{\text{Gaussian}}^2(\theta, \phi) \sin(\theta) d\theta d\phi = \int_0^{2\pi} \int_0^\pi G_{\text{Taylor}}^2(\theta, \phi) \sin(\theta) d\theta d\phi \quad (16)$$

where θ is the polar angle, ϕ is azimuth angle, G_{Gaussian} and G_{Taylor} are normalized one-way antenna patterns of Gaussian and Taylor, respectively. The effective -3 -dB beamwidth $\theta_{b,e}$ of ideal Gaussian antenna pattern can be calculated from the actual -3 -dB beamwidth of the one-way Taylor antenna pattern by multiplying a scale factor α

$$\theta_{b,e} = \alpha \theta_{b,\text{Taylor}}. \quad (17)$$

The scale factor α is analytically computed by (16). The left-hand side in (16) is

$$\int_0^{2\pi} \int_0^\pi G_{\text{Gaussian}}^2(\theta, \phi) \sin(\theta) d\theta d\phi \simeq \frac{\pi}{8 \ln 2} \theta_{b,e}^2. \quad (18)$$

The right-hand side in (16) is (19), as shown at the bottom of the page, where A and σ are given from the designed parameters of the Taylor distribution [23], and D is the length of the antenna. The -3 -dB beamwidth of the Taylor distribution $\theta_{b,\text{Taylor}}$ is

$$\theta_{b,\text{Taylor}} = \frac{2}{\pi} \frac{\sigma \lambda}{D} \sqrt{\pi^2 A^2 - \text{arccosh}^2\left(\frac{\cosh(\pi A)}{\sqrt{2}}\right)}. \quad (20)$$

Thus, α is given from (17)–(20), that is (21), as shown at the bottom of the page.

The important thing in (21) is that α depends on only A determined from the designed sidelobe level. For the DPR, the design sidelobe ratio corresponding to the maximum sidelobe level is assumed to be -35 dB, which gives $\alpha = 0.9916$. Hereafter, the beamwidths in cross-track and along-track directions obtained from the external calibration are computed as the effective beamwidth used in (1). Note that since DPR is a phased array radar and scans in cross-track direction, the cross-track beamwidth is standardized by multiplying $\cos \theta_s$ [24] considering the beam direction during the external calibration, where θ_s indicates scan angle of the DPR.

D. Summary of Calibration Method

The improvements in calibration realized from the PR calibration are summarized in Table III. The ability to calibrate the DPR with pulse waveform with a high PRF enables the external calibration without relying much on the parameter values measured at the FEPT. Direct measurements of the transmitted power of pulse waves from the ARC improve the accuracy of the calibration. The higher sampling resolution data received by the ARC clearly capture the waveform of radar's transmitted pulses.

Regarding the analysis for the external calibration, we re-examined the antenna pattern model and the fitting method for estimating the radar's antenna pattern. For the antenna pattern model, the Taylor distribution has been used to match the model between the fitting and the hardware design of the radar. We adopt the 2-D nonlinear fitting with the Levenberg–Marquart method in linear scale, which enables estimates of the radar's antenna parameter more accurately.

V. CONFIGURATIONS OF THE EXTERNAL CALIBRATION

External calibration of the DPR basically follows that described in T03 and is performed typically ten times out of

$$\int_0^{2\pi} \int_0^\pi G_{\text{Taylor}}^2(\theta, \phi) \sin(\theta) d\theta d\phi \simeq \left(\frac{4\pi A \sinh(4\pi A) - \cosh(4\pi A) + 32\pi A \sinh(2\pi A) - 16\cosh(2\pi A) + 17 + 24\pi^2 A^2}{64\pi \cosh^4(\pi A)} \right) \left(\frac{\sigma \lambda}{D} \right)^2 \quad (19)$$

$$\alpha = \sqrt{\ln 2 \left(\frac{4\pi A \sinh(4\pi A) - \cosh(4\pi A) + 32\pi A \sinh(2\pi A) - 16\cosh(2\pi A) + 17 + 24\pi^2 A^2}{32 \cosh^4(\pi A) \left(\pi^2 A^2 - \text{arccosh}^2\left(\frac{\cosh(\pi A)}{\sqrt{2}}\right) \right)} \right)} \quad (21)$$

TABLE IV
ANALYSIS PERIOD FOR DETERMINING CALIBRATION PARAMETERS OF THE DPR LEVEL-1 PRODUCTS IN V5

Item	Beginning of analysis period	End of analysis period	Remark
FCIF_LUT	March 9, 2014	August 19, 2015	All internal calibration.
δEIRP	May 16, 2015	December 4, 2016	Except for external calibration using inappropriate coaxial cable. Only Pulse calibration. Rx: Only CW calibration. Tx: All external calibrations.
δS_a	November 7, 2016	December 4, 2016	
θ_a and θ_c	June 10, 2014	November 22, 2015	

about 100 overpass events a year above the Tsukuba Space Center, Tsukuba, Japan (36° 03' 56.3" N, 140° 07' 40.0" E) where the DPR-ARC is installed. The external calibrations in spring and autumn are preferred because the DPR-ARC has somewhat of a temperature characteristic. As a suitable season approaches, we coordinate the external calibration's schedule with NASA and conduct the external calibration with the orbital prediction provided by NASA.

In the past, we encountered many unexpected troubles. For example, we found unusual temperature dependence of cable loss in the two coaxial cables that connected the DPR-ARC's Tx and Rx systems. They changed by about 1 dB in about 10 min, especially in low-temperature seasons. Thereby, those cables were replaced by a new type of coaxial cables in May 2015, and only the results of calibration after the replacement were used for the evaluation of δEIRP .

In the DPR Rx system calibration, the different responses of the DPR Rx system depending on the waveform should be considered. As described in Section IV-B, the pulse calibration is preferred over the CW calibration because of the consistency with the internal calibration. In the PR's calibration, although the pulse calibration had been conducted in the transponder mode, the bias error was larger than the CW calibration [17]. Therefore, the CW calibration was prioritized to determine the correction values of the PR. In the DPR's calibration, the CW calibration had been conducted until October 2016 because we assumed to be the same between the response of the DPR to CWs and pulse waves and believed that the P_{ic} in (14) could be ideally evaluated as much of P_{ip} . In fact, the CW calibration was simpler, more stable, and reproducible than the pulse calibration and had been prioritized. However, as the procedure of the DPR's pulse calibration had matured, we switched to the pulse calibration from the CW calibration. Then, we found a difference between the results of CW calibration and pulse calibration to be about 0.7 dB, that is, P_{ic} was overestimated by about 0.7 dB relative to the P_{ip} . Consequently, we have prioritized the pulse calibration.

Note that θ_a and θ_c are also provided by analyzing the external calibration data. To evaluate the beamwidths, the different responses in the DPR Rx system and unusual characteristics of the coaxial cable had to be taken into consideration. Fortunately, they did not affect the estimated beamwidths significantly. In fact, the impact of the different responses in the DPR Rx system was negligible because the beamwidths obtained from CW calibration and pulse calibration agreed well within 2%. The unusual characteristics of the coaxial cable were also negligible because the absolute power is

irrelevant to the estimation of the beam patterns. However, the possible errors associated with the above-mentioned problems were taken into account when averaging the results of the external calibration as listed in Table IV.

VI. RESULTS AND DISCUSSION

A. Evaluation of the External Calibration

As described in Sections II and IV, magnitudes of δEIRP and δS_a calculated from (3)–(13) are obtained from each external calibration. The DPR Tx system's postlaunch correction factor C_t and that of DPR Rx system C_r are determined from the statistical results of the Tx and Rx systems

$$C_t = -\overline{\delta\text{EIRP}} \text{ and } C_r = \overline{\delta S_a} \quad (22)$$

where over line denotes the average of variable. For the DPR's calibration, the DPR's antenna gains measured at the FEPT are used for G_{t0} in (9) and G_{r0} in (11), and FCIF__LUT₀ in (13) was replaced to the statistical results of the internal calibration obtained from the analysis period as listed in Table IV. To determine C_t and C_r for the DPR level-1 products in V5, we evaluated DPR's external calibration data from May 16, 2015 to December 4, 2016 for the Tx system and from November 7, 2016 to December 4, 2016 for the Rx system. θ_a and θ_c were determined as the statistical results of the data from June 10, 2014 to November 22, 2015 as listed in Table IV.

B. Case Study

Fig. 7 shows a result of the KuPR Rx system calibration with the ARC on December 2, 2016. Fig. 7(a) shows the distribution of the KuPR's received powers of signals from the KuARC's transmitted power at various incidence angles relative to the beam center measured by the KuPR. They were measured at different scan angles and different along-track positions. Actual data thus collected are plotted at the direction relative to the beam center in this combined representation. The cross-track angle shown in Fig. 7(a) is the actual scan angle. As shown in Fig. 7(a), the powers can be measured only at discrete angles. Fig. 7(b) shows the KuPR's received power after fitting a model distribution to the actual data. From the fit surface, the magnitude of the peak power was estimated to be -81.44 dBm whereas the maximum of the original data was -81.51 dBm. In addition, θ_a and θ_c for the KuPR Rx antenna were estimated to be 0.692° and 0.704° , respectively. Fig. 7(c) and (d) shows the results of applying the same method for the KuPR Tx system. Fig. 7(c) shows the distribution of the KuARC's received powers of signals from

TABLE V
STATISTICAL RESULTS OF THE EXTERNAL CALIBRATION WITH THE DPR PRODUCTS IN V5. THE RESULTS ARE OBTAINED FROM PERIODS IN TABLE IV AND ARE ADDITIONALLY ANALYZED BY JUNE 13, 2018

Item	KuPR	S.D.	KaPR	S.D.
EIRP(RADAR) – EIRP(ARC)	0.00 dB	0.226 dB	–0.01 dB	0.159 dB
$S_a(\text{RADAR}) - S_a(\text{ARC})$	–0.07 dB	0.152 dB	–0.32 dB	0.334 dB
$\theta_{a,Tx}$	0.703°	0.0137°	0.695°	0.0116°
$\theta_{a,Rx}$	0.696°	0.0072°	0.697°	0.0132°
θ_a	0.699°	–	0.696°	–
$\theta_{c,Tx}$	0.713°	0.0079°	0.712°	0.0086°
$\theta_{c,Rx}$	0.707°	0.0063°	0.737°	0.0101°
θ_c	0.710°	–	0.724°	–

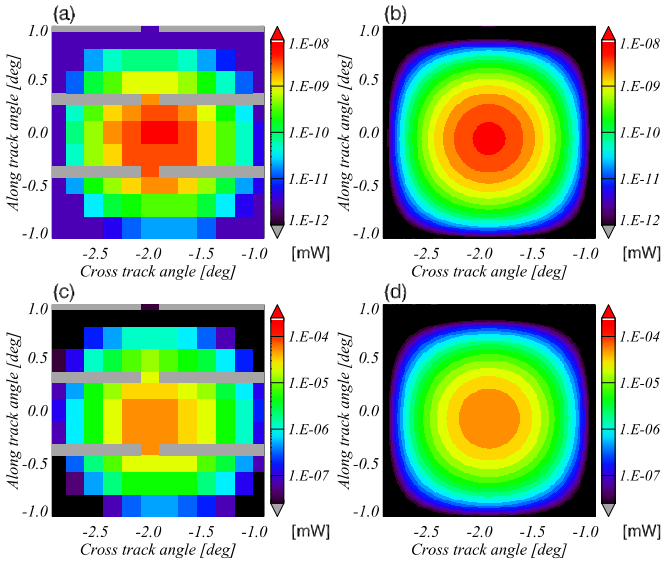


Fig. 7. Example of fitting for the KuPR's and KuARC's received power in linear scale during the external calibration on December 2, 2016. (a) Observed KuPR's received power. (b) Estimated KuPR's received power after the fitting. (c) Observed KuARC's received power. (d) Estimated KuARC's received power after the fitting. Horizontal axis denotes the cross-track direction ($^{\circ}$) and vertical axis denotes the along-track direction ($^{\circ}$).

KuPR's transmitted power, and Fig. 7(d) shows the KuARC's received powers after fitting. The magnitude of the peak power was estimated to be -40.07 dBm whereas the maximum of the original data was -40.30 dBm. For the KuPR Tx antenna, θ_a and θ_c were estimated to be 0.696° and 0.711° , respectively.

C. Statistical Analysis

From the results of several external calibrations, we determined that KuPR's C_t was -0.29 dB, KaPR's C_t was -0.95 dB, KuPR's C_r was 0.13 dB, and KaPR's C_r was 1.13 dB. The standard deviations of these estimates were less than 0.3 dB. Since a negative value of the C_t indicates that P_{t0} was overestimated, applying the negative C_t decreases the P_{t0} . In contrast to C_t , applying the positive C_r decreases the P_{r0} because a positive value of the C_r implies that P_{r0} was overestimated. C_t and C_r were determined from the results of a few external calibrations listed in Table IV.

Figs. 8 and 9 show the trends of the latest calibration with V5 of the standard DPR products which employ C_t and C_r . The statistical results of the calibration are summarized in Table V. Table V also shows that differences in EIRP and S_a between DPR and ARC are less than ± 0.5 dB and their standard deviations are smaller than 0.4 dB. These statistics imply that the correction values are reliable even though the number of the pulse calibrations is not significant and that the calibrations of both KuPR and KaPR satisfy the required accuracy of better than ± 1 dB.

A point of concern is that the standard deviation of the difference in S_a between KaPR and ARC is slightly larger than the others, which may arise from the estimation error in atmospheric attenuation loss. As described in Section IV-A, we use the atmospheric attenuation loss estimated by the Global Objective Analysis Data. The magnitude of the atmospheric attenuation loss is about -0.1 dB for Ku-band and -0.3 dB for Ka-band, and the standard deviation of that is 0.02 dB for Ku-band and 0.11 dB for Ka-band. The standard deviation of 0.334 dB in the S_a difference between KaPR and ARC (i.e., $S_a(\text{RADAR}) - S_a(\text{ARC})$) is three times larger than that of the atmospheric attenuation loss for Ka-band. Moreover, if the variation in the calibration results of the KaPR Rx system depends on the estimation error of atmospheric attenuation loss, then the calibration of the KaPR Tx system should also be affected by the same magnitude, but Tx's standard deviation of 0.152 dB is about half of Rx's standard deviation, which suggests that the large variation of the KaPR's S_a difference is a specific issue for calibration of the KaPR Rx system.

The KaPR has two modes of operations called "KaMS" and "KaHS" depending on the pulsewidth. The KaMS transmits $1.6 \mu\text{s}$ of pulsewidth (i.e., the range resolution is 250 m) with viewing angles that are matched to those of the inner swath of the KuPR, while the KaHS transmits $3.2 \mu\text{s}$ of pulsewidth (i.e., the range resolution is 500 m) and interlaces within the KaMS's beams [3], [18]. When we conduct the pulse calibration, corresponding pulse waves should be received by each kind of beams of the KaPR. In other words, the KaARC should transmit $1.6\text{-}\mu\text{s}$ pulse waves for KaMS and $3.2\text{-}\mu\text{s}$ pulse waves for KaHS. If the KaHS received $1.6\text{-}\mu\text{s}$ pulse wave, the intensity measured by the KaHS is biased because its BPF is matched for $3.2\text{-}\mu\text{s}$ pulse waves. Although the KaARC

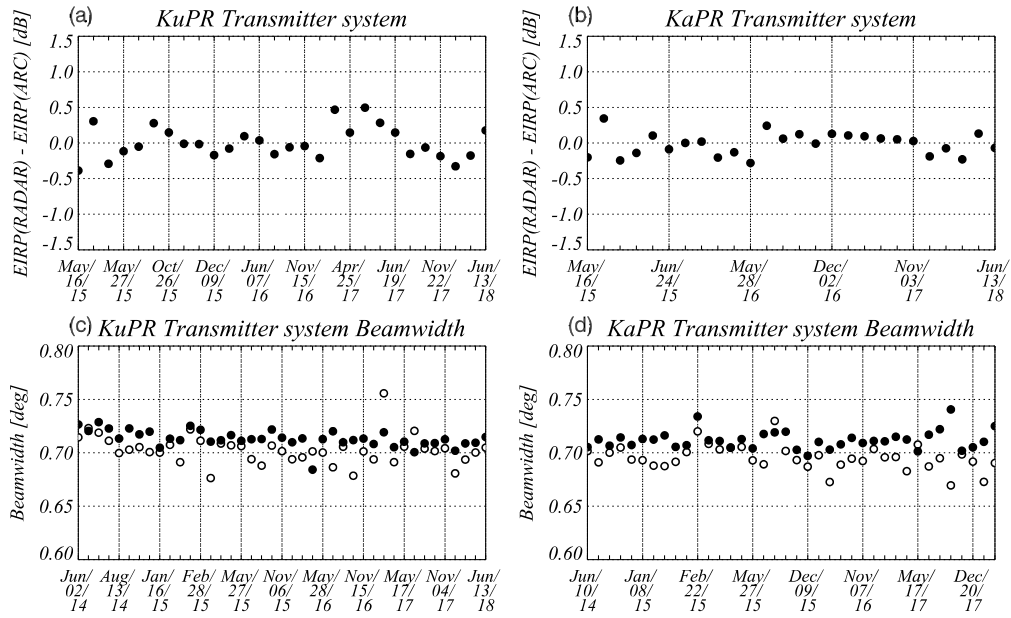


Fig. 8. Results of the external calibration for DPR Tx system. (a) EIRP(RADAR) – EIRP(ARC) (dB) of the KuPR. (b) Same as (a), but the KaPR. Horizontal axis denotes the date of the external calibration. (c) Tx beamwidth (°) of the KuPR. (d) Same as (c), but the KaPR. Open and filled circles indicate the along-track beamwidth and the cross-track beamwidth, respectively.

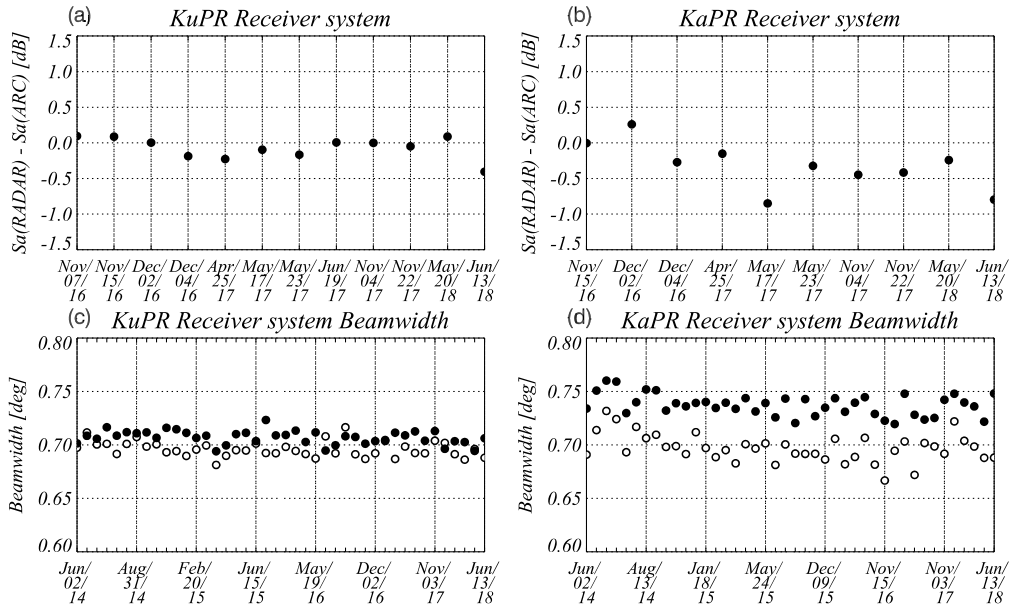


Fig. 9. Results of external calibration for DPR Rx system. (a) S_a (RADAR) – S_a (ARC) (dB) of the KuPR. (b) Same as (a), but the KaPR. Horizontal axis denotes the date of external calibration. (c) Rx beamwidths of the KuPR. (d) Same as (c), but the KaPR. Circles in (c) and (d) indicate the same as Fig. 8.

is designed to be able to control the pulsewidth automatically with prepared settings, we evaluate only the KaMS’s received power because of the simplicity and operability of the external calibration.

Furthermore, the magnitude of the S_a difference between KaPR and ARC turned out to be larger than expected even after the correction values are applied. The cause of this large correction factor seems to stem from the change of the KaPR’s parameters with time [Fig. 9(b)]. The variation of the KaPR’s overall gain is also recognized in the decreasing trend of the normalized radar cross sections (NRCS; σ^0) of

ocean surface if the constant radar parameters are used to calculate them. In fact, KaPR’s σ^0 has gradually decreased by about 1 dB over the approximately five-year period since the beginning of normal mission operations in May 2014 (not shown). Such trends are consistent with the change of the S_a difference and are probably caused by a change of the KaPR Rx system characteristic because the trend appears only in the S_a difference and not in the EIRP difference. To mitigate the estimation error for the precipitation rate caused by the changing trend, the DPR level-2 algorithm compensates for it by introducing an “adjustment factor” that varies with

time [18]. Regarding the beamwidth, θ_a and θ_c in (1) are calculated by using Tx and Rx beamwidth which are separately estimated with the external calibration data, that is,

$$\theta_a = \sqrt{\theta_{a,Tx} \cdot \theta_{a,Rx}} \text{ and } \theta_c = \sqrt{\theta_{c,Tx} \cdot \theta_{c,Rx}} \quad (23)$$

where $\theta_{a,Tx}$ is the beamwidth of Tx and $\theta_{a,Rx}$ is the beamwidth of Rx in the along-track direction, $\theta_{c,Tx}$ and $\theta_{c,Rx}$ are those of the cross-track direction. We employed θ_a and θ_c in the V5 of DPR level-1 products by averaging the results of the external calibration until 2016 as listed in Table IV. Then, KuPR's θ_a was 0.701° , KaPR's θ_a was also 0.701° , KuPR's θ_c was 0.713° , and KaPR's θ_c was 0.726° . Their standard deviations were less than 0.014° . Since the beamwidths were measured to be 0.719° for KuPR's θ_a , 0.699° for KaPR's θ_a , 0.696° for KuPR's θ_c , and 0.718° for KaPR's θ_c at the FEPT, KuPR's θ_a decreased 2.6%, KaPR's θ_a increased 0.2%, KuPR's θ_c increased 2.5%, and KaPR's θ_c increased 1.2% comparing to the beamwidths obtained at the FEPT. The latest results of the θ_a and θ_c as listed in Table V agree with the DPR level-1 values within the 0.7% for both KuPR and KaPR. We can conclude that θ_a and θ_c adopted in the DPR products in V5 have no trend and are reliable. It is worth noting that Kanemaru *et al.* [20] estimated θ_c from sea surface echoes at oblique incidence angles. Their results agree very well with our results within 0.006° .

D. Impacts on Z_m and σ^0

With the new parameters of calibration, Z_m in (1) increased by about 1.3 dB for the KuPR and 1.2 dB for the KaPR from the corresponding Z_m calculated with the parameters obtained at the FEPT. The increase of Z_m results in a change of the minimum detectable precipitation rate R_{\min} . In the case of the DPR, R_{\min} is given by the minimum detectable radar reflectivity Z_{\min}

$$R_{\min} = a^{(-1/b)} Z_{\min}^{(1/b)} \quad (24)$$

where a and b are the coefficients of the Z - R relation: $Z = aR^b$ in linear scale.

Since the DPR can measure only received power P_r in (1) which is the sum of echo signal power P_s from precipitation echoes and background noise power P_n in linear scale

$$P_r = P_s + P_n \quad (25)$$

we need to subtract P_n from P_r to obtain P_s . Precipitation echoes are judged to be present when P_r is clearly greater than P_n . We define Z_t as the threshold value of Z_m calculated by using (1), which corresponds to the threshold of P_r for the detection of precipitation. Since both P_r and P_n are measured and averaged in logarithmic scale, if Z_n is defined as noise equivalent radar reflectivity, $10\log_{10}(Z_t)$ is given by the sum of $10\log_{10}(Z_n)$ and the expected fluctuations of P_r and P_n as follows:

$$10\log_{10}(Z_t) = 10\log_{10}(Z_n) + m\sqrt{\sigma_t^2 + \sigma_n^2} \text{ in [dB]} \quad (26)$$

where σ_t is the standard deviation of fluctuations in the P_r , σ_n is that of P_n , and m is a threshold related to the reliability

of P_r and P_n against those fluctuations caused by Rayleigh fading. σ_t and σ_n are given by the following formulas [19]:

$$\sigma_t = \frac{5.57}{\sqrt{N}} \text{ and } \sigma_n = \frac{5.57}{\sqrt{M}} \text{ in [dB]}. \quad (27)$$

Here, N is the sampling number of P_r at each range-bin, and M is the sampling number of P_n .

As described in (1), since radar reflectivity factor (Z) is proportional to DPR's received signals, Z_n is required to be subtracted from Z_t just as P_n is subtracted from P_r to obtain P_s , and Z_{\min} is given as follows in linear scale:

$$Z_{\min} = Z_t - Z_n. \quad (28)$$

Thus, R_{\min} is expressed by using Z_n and the sampling numbers of DPR as follows:

$$R_{\min} = a^{(-1/b)} [Z_n \{10^{(m\sqrt{\sigma_t^2 + \sigma_n^2}/10)} - 1\}]^{(1/b)}. \quad (29)$$

In this study, Z_n is evaluated by averaging the normal observation data in May 2017 overland when no rain is detected by the DPR level-2 (precipitation-estimation) algorithm. Since the background noise overland when no rain is detected is the highest noise in the normal observation, it is preferred to evaluate the worst case for the precipitation detection. Typical values of N and M are used for R_{\min} when the satellite is at its nominal altitude of 407 km. Consequently, KuPR's Z_{\min} is 12.17 dBZ, KaMS's Z_{\min} is 15.61 dBZ, KaHS's Z_{\min} is 10.40 dBZ, KuPR's R_{\min} is 0.21 mm/h, KaMS's R_{\min} is 0.34 mm/h, and KaHS's R_{\min} is 0.16 mm/h by using parameters which were applied in the DPR's design ($a = 200$, $b = 1.6$, and $m = 2$) and P_n was assumed for CW ($P_{r,\text{noise}}$ in Appendix A) to match the definition with the P_n measured by CW of external power source in ground tests before launch. On the other hand, in the DPR level-2 algorithm, an assumption of Z - R relationship and m differ from the parameters used in the DPR's design. In the DPR level-2 V6 algorithm, we consider the P_n is assumed for pulse wave same as precipitation echoes ($P_{r,\text{prcp}}$ in Appendix A) and use $a = 298.84$, $b = 1.38$ for the estimation of stratiform precipitation [25] and $m = 2.5$ [26], which yields that, KuPR's Z_{\min} is 15.46 dBZ, KaMS's Z_{\min} is 19.18 dBZ, KaHS's Z_{\min} is 13.71 dBZ, KuPR's R_{\min} is 0.21 mm/h, KaMS's R_{\min} is 0.39 mm/h, and KaHS's R_{\min} is 0.16 mm/h. The summary is listed in Table VI.

The measured σ^0 of the Earth's surface is one of the effective indexes to verify the DPR's calibration objectively. Fig. 10 shows the results of statistical analysis of the measured σ^0 in the tropical regions (i.e., from 36° N to 36° S) over ocean when no rain is detected by the DPR level-2 algorithm. Fig. 10(a) shows the monthly averages of the σ^0 in June 2014 when the DPR and PR concurrently worked. In the evaluation, we use the V5 of standard DPR level-2 products. Note that the frequency of the PR (13.8 GHz) is effectively identical to that of the KuPR (13.6 GHz). The parameters of calibration for the PR were re-examined by taking advantage of the results of the DPR calibration (see Appendix B) and were employed in the TRMM version 8 (V8) of standard PR level-2 products. Fig. 10(b) shows the difference of the measured σ^0 between KuPR and PR over

TABLE VI
PARAMETERS FOR CALCULATING Z_{\min} AND R_{\min} AND THOSE RESULTS

Instrument	N	M	a	b	m	Assumption of P_n	Z_{\min} [dBZ]	R_{\min} [mm/h]
KuPR	102	1008	200	1.6	2.0	CW	12.17	0.21
KuPR	102	1008	298.84	1.38	2.5	Pulse	15.46	0.21
KaMS	106	968	200	1.6	2.0	CW	15.61	0.34
KaMS	106	968	298.84	1.38	2.5	Pulse	19.18	0.39
KaHS	106	427	200	1.6	2.0	CW	10.40	0.16
KaHS	106	427	298.84	1.38	2.5	Pulse	13.71	0.16

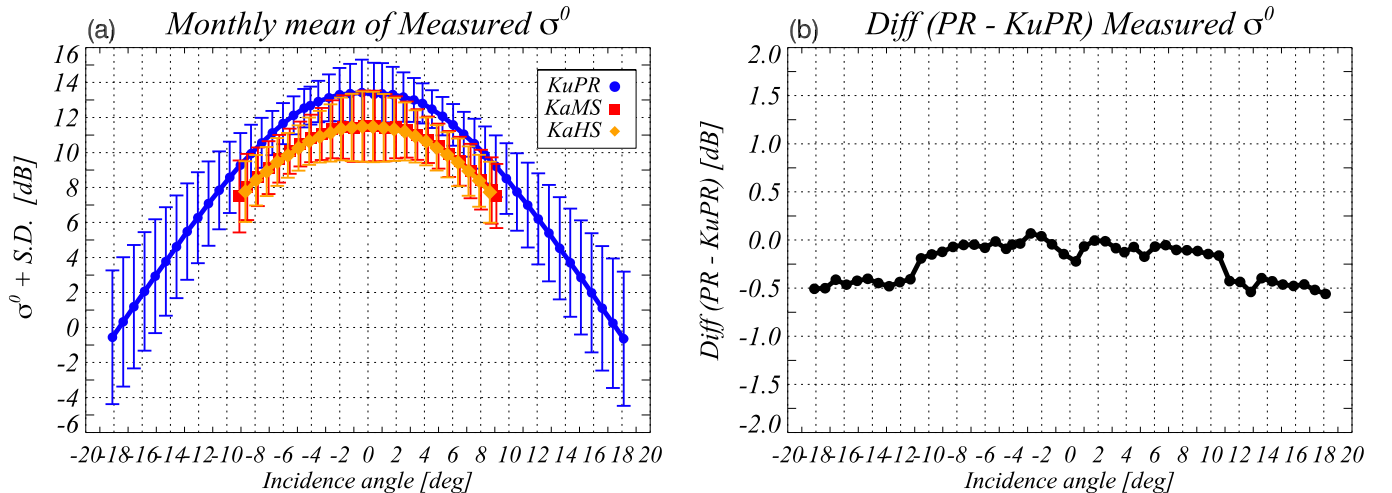


Fig. 10. Statistics of measured σ^0 over ocean when no rain is detected by the DPR level-2 algorithm in June 2014. (a) Monthly average of σ^0 . Lines indicate KuPR (blue), KaMS (red), and KaHS (orange). Horizontal axis denotes incidence angle ($^\circ$) and vertical axis denotes measured σ^0 (dB). Error bars indicate ± 1 standard deviation (dB) for each incidence angle. (b) Difference in σ^0 (dB) between the PR and KuPR.

ocean in the tropical regions. The result indicates the PR's σ^0 agrees well with KuPR's σ^0 , especially at the incidence angles within around $\pm 11^\circ$. The biases at incidence angle larger than $\pm 11^\circ$ are caused by the PR's sparse range sampling intervals that underestimate σ^0 . The PR oversamples the Earth's surface echoes with a 125-m interval when the incidence angle is less than $\pm 11^\circ$, while it samples only with a 250-m interval at large incidence angles and misses the surface echo peak [16], [20], thereby resulting in the underestimation of σ^0 in the outer regions. In contrast to the PR, the DPR oversamples the Earth's surface echoes in all angles so that no discontinuity is expected.

VII. CONCLUSION

The new radar parameters of the DPR are determined by analyzing four years of calibration data after launch, whose results are employed in V5 of standard DPR level-1 products released in May 2017. The calibration method basically follows the method described in T03 for the PR's calibration. However, we improve the calibration equipment and analysis method to accurately calibrate the DPR as shown in Table III. Regarding the equipment, the new ARCs and its new functions are introduced. Since the response of the radar Rx's was found to depend on the waveform, the ARCs were improved in such a way that the external calibration can be performed with both continuous and pulse waves.

Furthermore, we improve the analysis method for the external calibration. With regard to the antenna pattern estimation using the data obtained by the external calibration, fitting a Gaussian distribution in logarithmic scale was adopted in the PR's calibration by T03 with the assumption that the difference between Gaussian and Taylor distributions was small. However, we found that the difference was not negligible when the fitting area was changed. Therefore, we use the antenna pattern estimated with a Taylor distribution to realize more accurate calibration. The difference in antenna pattern between the Gaussian and Taylor distributions is considered to determine the appropriate beamwidths used in the radar equation by introducing the effective beamwidths that the energy of the Taylor antenna pattern is equivalent to that of the Gaussian antenna pattern.

The new calibration results change the Tx system gain by -0.29 dB for the KuPR and by -0.95 dB for the KaPR. Similarly, in the Rx system gains are corrected by 0.13 dB for the KuPR and by 1.13 dB for the KaPR. These values imply that both DPR's transmitted and received powers determined by the FEPT before launch were overestimated. Regarding the beamwidth, the KuPR's and KaPR's along-track beamwidths are determined to be 0.701° , and the KuPR's and KaPR's cross-track beamwidths are 0.713° and 0.726° , respectively. With the new parameters of calibration, Z_m increased by about 1.3 dB for the KuPR and by 1.2 dB for the KaPR. As a result,

the minimum detectable radar reflectivities become 15.46, 19.18, and 13.71 dBZ for KuPR, matched beam of KaPR and high-sensitivity beam of KaPR, respectively, overland when no rain is detected by the DPR level-2 algorithm during May 2017. As shown in Appendix B, the parameters of the PR's calibration are re-examined in a similar way as in the DPR's calibration. As a result, the new PR's σ^0 agrees well with KuPR's. The re-examination of the PR's calibration improves the accuracy and consistency of calibration with the DPR's calibration.

By examining the four years of calibration data, we determined the new calibration parameters of the DPR. The analysis of calibration data also shows that the DPR's performance is very stable and that the error in the calibration accuracy is within ± 1 dB. Nevertheless, the calibration bias of the KaPR Rx system is slightly larger than that of the KuPR Rx system and shows a trend. We speculate that the trend is caused by a change in the characteristics of the KaPR Rx system and not of the KaPR Tx system because the trend of the KaPR Tx system is stable. More detailed investigation with long-term data is necessary.

APPENDIX A DEFINITION OF P_r

The waveform of pulse signals received by the DPR changes in the BPF because its bandwidth is designed to be somewhat narrower than the spectral width of the transmitted pulse in order to maximize the signal-to-noise ratio. As a result, when we calibrate the DPR's Rxs, we have to take into account the difference of its response to continuous and pulse waves. Calibration is carried out with a signal with constant amplitude, but precipitation echoes fluctuate according to the Rayleigh fading. Since the received signal is log-detected, the bias caused by fading with log-detection must be taken into account as well. The relation between the received power at the antenna feed and the value recorded by using the FCIF-LUT can be expressed as follows for four kinds of waves:

$$P_{r,\text{prcp}} = P_{\text{ip}} - G_{\text{RS}} - L_e + L_p + L_f - C_r \quad (\text{A1})$$

$$P_{r,\text{pls}} = P_{\text{ip}} - G_{\text{RS}} - C_r \quad (\text{A2})$$

$$P_{r,\text{cw}} = P_{\text{ic}} - G_{\text{RS}} + L_p - C_r \quad (\text{A3})$$

$$P_{r,\text{noise}} = P_{\text{ic}} - G_{\text{RS}} + L_p + L_f - C_r. \quad (\text{A4})$$

As shown in (A2), since the FCIF-LUT is calibrated with pulse waves, we only need to consider the Rx's gain G_{RS} and the correction factor C_r to relate the input power P_{ip} and the recorded power $P_{r,\text{pls}}$ in the case of pulse input. The Rx system's response to CWs differs from that to the pulse waves by L_p where L_p is the peak loss of the pulse wave when it goes through the BPF. Because the FCIF-LUT is constructed with the measurement of peak power of calibration pulses, L_p must be included as shown in (A3) to relate the input power of CW P_{ic} and the corresponding recorded power $P_{r,\text{cw}}$. In the case of precipitation echoes, we measure pulse waves that consist of the integral of backscattered pulse echoes with fluctuation. In other words, the total energy of the echo pulse is measured. Therefore, the energy loss L_e by the BPF must be included

in addition to the correction L_f due to the log-detection of fading signal as shown in (A1) to relate the input power P_{ip} and the recorded value $P_{r,\text{prcp}}$. In the case of noise, $P_{r,\text{noise}}$ is calculated from $P_{r,\text{cw}}$ by compensating the underestimation due to the fading signal. The following values were determined by examining the calibration data taken before launch: L_e is -1.81 dB for KuPR and KaMS, -1.53 dB for KaHS. L_p is -0.76 dB for KuPR and KaMS, -0.30 dB for KaHS. L_f is 2.51 dB for KuPR and KaPR.

APPENDIX B CALIBRATION OF THE TRMM PR

JAXA released TRMM version 7 (V7) of the PR products [27] in July 2011 and TRMM V8 of the PR products as GPM products in October 2017. The products in TRMM V8 employ the new calibration parameters obtained by re-examining the PR's calibration; then the PR was calibrated by the DPR-ARC with the method described in this article. Moreover, we also reevaluated all calibration results obtained from the PR-ARC with the new evaluation tools developed in the works of the DPR's calibration. For the external calibration, the pulse calibration was carried out for the PR using the DPR-ARC which can also operate at PR's frequencies of 13.796 (f1) and 13.802 GHz (f2). Thus, both DPR and PR were calibrated with the same calibrator. In fact, we conducted the external calibration of the PR with the DPR-ARC at the Kansai branch of NICT ($34^\circ 42' 43.6''$ N, $134^\circ 57' 06.6''$ E) from September to October in 2014. Since the TRMM satellite had a solar asynchronous orbit with an orbital inclination angle of approximately 35° [14], the Kobe branch of NICT was a suitable place to calibrate the PR in terms of visiting frequency.

As a result, the correction value of the PR Rx B-side system (C_{rB}) was 1.9 dB, and C_r of the PR was -0.92 dB. Note that the PR's Rx system was switched from A- to B-side system in June 2009 on account of A-side Rx system issue [28]. Since the A-side system was not directly calibrated with the DPR-ARC, the correction value of the PR Rx A-side system (C_{rA}) was determined by using results of DPR-ARC and PR-ARC by taking a difference in results between those into account; then, C_{rA} was given to be -0.37 dB. Other parameters of calibration such as pulsewidth and beamwidth were also reevaluated. As a result, θ_a and θ_c were estimated to be 0.692° and 0.708° . For the pulsewidth, the DPR-ARC measured the pulse waveform of the PR, and the pulse-like response of the PR was reconstructed from sea surface echo data [20]. From those results, τ was obtained to be $1.40 \mu\text{s}$ for the A-side and $1.45 \mu\text{s}$ for the B-side system.

With the new parameters, the Z_m increased by about 1.1 dB relative to the V7 values. To evaluate the Z_{min} and R_{min} , the same methods described in Section VI-D were used as well as the DPR and we calculated them for the satellite altitudes of 350 and 402.5 km taking into account the TRMM boost [28]. As a result, Z_{min} was 19.34 dBZ in 350-km altitude and 20.21 dBZ in 402.5-km altitude. Corresponding R_{min} was 0.40 mm/h in 350-km altitude and 0.47 mm/h in 402.5-km altitude. Note that Z_n was evaluated by averaging the normal observation data in July 2001 for 350-km altitude and

June 2014 for 402.5-km altitude. Since TRMM V8 of the PR algorithm is basically same as the DPR level-2 V6 algorithm, the parameters for calculating Z_{\min} and R_{\min} are same as those of DPR, thus, $a = 298.84$, $b = 1.38$, and $m = 2.5$. Although the Z_{\min} was degraded by 1.2 dB ($= 20\log(402.5/305)$) due to the changes in the satellite altitude from 350 to 402.5 km as reported by Takahashi and Iguchi [29], our results slightly differ from them. One reason is the difference in sensitivity between A- and B-side system [28].

Regarding σ^0 , PR's σ^0 agreed well with KuPR's σ^0 within 0.02 dB (i.e., KuPR's σ^0 was slightly larger than PR's σ^0) in incidence angles less than $\pm 11^\circ$ as shown in Fig. 10(b). The agreement supports that the re-examination of the PR's calibration has worked well.

ACKNOWLEDGMENT

The authors are deeply grateful to M. Kojima and Dr. T. Miura of the Japan Aerospace Exploration Agency (JAXA), Tsukuba, Japan, H. Hanado of the National Institute of Information and Communications Technology (NICT), Koganei, Japan, H. Kai, T. Higashiwatoko of the Remote Sensing Technology Center of Japan (RESTEC), Tsukuba, Japan, Dr. M. Okumura of I-NET Corporation, Yokohama, Japan, and Dr. S. Seto of Nagasaki University, Nagasaki, Japan, for providing very important information and comments to the calibration and dual-frequency precipitation radar (DPR) level-2 algorithm. They would also like to express the deepest appreciation to Dr. K. Fujii of NICT, for measuring the antenna gain of the active radar calibrators (ARCs) against the national standard, and appreciate helpful review comments from anonymous reviewers.

REFERENCES

- [1] A. Y. Hou *et al.*, "The global precipitation measurement mission," *Bull. Amer. Meteorological Soc.*, vol. 95, no. 5, pp. 701–722, May 2014, doi: [10.1175/BAMS-D-13-00164.1](https://doi.org/10.1175/BAMS-D-13-00164.1).
- [2] G. Skofronick-Jackson *et al.*, "The global precipitation measurement (GPM) mission for science and society," *Bull. Amer. Meteorol. Soc.*, vol. 98, no. 8, pp. 1679–1695, Aug. 2017, doi: [10.1175/BAMS-D-15-00306.1](https://doi.org/10.1175/BAMS-D-15-00306.1).
- [3] M. Kojima *et al.*, "Dual-frequency precipitation radar (DPR) development on the global precipitation measurement (GPM) core observatory," *Proc. SPIE*, vol. 8528, Nov. 2012, Art. no. 85281A, doi: [10.1117/12.976823](https://doi.org/10.1117/12.976823).
- [4] K. Furukawa *et al.*, "Satellite system test status of the dual-frequency precipitation radar on the global precipitation measurement core spacecraft," in *Proc. IEEE Int. Geosci. Remote Sens. Symp. - IGARSS*, Jul. 2013, pp. 1143–1146.
- [5] T. Kubota *et al.*, "Evaluation of precipitation estimates by at-launch codes of GPM/DPR algorithms using synthetic data from TRMM/PR observations," *IEEE J. Sel. Topics Appl. Earth Observ. Remote Sens.*, vol. 7, no. 9, pp. 3931–3944, Sep. 2014, doi: [10.1109/JSTARS.2014.2320960](https://doi.org/10.1109/JSTARS.2014.2320960).
- [6] T. Kubota *et al.*, "A statistical method for reducing sidelobe clutter for the ku-band precipitation radar on board the GPM core observatory," *J. Atmos. Ocean. Technol.*, vol. 33, no. 7, pp. 1413–1428, Jul. 2016.
- [7] T. Iguchi, "Dual-frequency precipitation radar (DPR) on the global precipitation measurement (GPM) mission's core observatory," in *Satellite precipitation measurement*. Cham, Switzerland: Springer, 2020, doi: [10.1007/978-3-030-24568-9_11](https://doi.org/10.1007/978-3-030-24568-9_11).
- [8] D. W. Draper, D. A. Newell, D. A. Teusch, and P. K. Yoho, "Global precipitation measurement microwave imager prelaunch hot load calibration," *IEEE Trans. Geosci. Remote Sens.*, vol. 51, no. 9, pp. 4731–4742, Sep. 2013, doi: [10.1109/TGRS.2013.2239300](https://doi.org/10.1109/TGRS.2013.2239300).
- [9] D. W. Draper, D. A. Newell, D. S. McKague, and J. R. Piepmeier, "Assessing calibration stability using the global precipitation measurement (GPM) microwave imager (GMI) noise diodes," *IEEE J. Sel. Topics Appl. Earth Observ. Remote Sens.*, vol. 8, no. 9, pp. 4239–4247, Sep. 2015, doi: [10.1109/JSTARS.2015.2406661](https://doi.org/10.1109/JSTARS.2015.2406661).
- [10] D. W. Draper, D. A. Newell, F. J. Wentz, S. Krimchansky, and G. M. Skofronick-Jackson, "The global precipitation measurement (GPM) microwave imager (GMI): Instrument overview and early on-orbit performance," *IEEE J. Sel. Topics Appl. Earth Observ. Remote Sens.*, vol. 8, no. 7, pp. 3452–3462, Jul. 2015, doi: [10.1109/JSTARS.2015.2403303](https://doi.org/10.1109/JSTARS.2015.2403303).
- [11] C. D. Kummerow *et al.*, "The evolution of the goddard profiling algorithm to a fully parametric scheme," *J. Atmos. Ocean. Technol.*, vol. 32, no. 12, pp. 2265–2280, Dec. 2015, doi: [10.1175/JTECH-D-15-0039.1](https://doi.org/10.1175/JTECH-D-15-0039.1).
- [12] M. Grecu *et al.*, "The GPM combined algorithm," *J. Atmos. Ocean. Technol.*, vol. 33, no. 10, pp. 2225–2245, Oct. 2016, doi: [10.1175/JTECH-D-16-0019.1](https://doi.org/10.1175/JTECH-D-16-0019.1).
- [13] T. Kubota *et al.*, "Global satellite mapping of precipitation (GSMAp) products in the GPM era," in *Satellite Precipitation Measurement*. Cham, Switzerland: Springer, 2020, doi: [10.1007/978-3-030-24568-9_20](https://doi.org/10.1007/978-3-030-24568-9_20).
- [14] J. Simpson, R. F. Adler, and G. R. North, "A proposed tropical rainfall measuring mission (TRMM) satellite," *Bull. Amer. Meteorol. Soc.*, vol. 69, no. 3, pp. 278–295, Mar. 1988.
- [15] C. Kummerow, W. Barnes, T. Kozu, J. Shiue, and J. Simpson, "The tropical rainfall measuring mission (TRMM) sensor package," *J. Atmos. Ocean. Technol.*, vol. 15, no. 3, pp. 809–817, Jun. 1998.
- [16] T. Kozu *et al.*, "Development of precipitation radar onboard the tropical rainfall measuring mission satellite," *IEEE Trans. Geosci. Remote Sens.*, vol. 39, no. 1, pp. 102–112, Jan. 2001.
- [17] N. Takahashi, H. Kuroiwa, and T. Kawanishi, "Four-year result of external calibration for precipitation radar (PR) of the tropical rainfall measuring mission (TRMM) satellite," *IEEE Trans. Geosci. Remote Sens.*, vol. 41, no. 10, pp. 2398–2403, Oct. 2003.
- [18] T. Iguchi *et al.* (2018). *GPM/DPR Level-2 Algorithm Theoretical Basis Document*. [Online]. Available: https://www.eorc.jaxa.jp/GPM/doc/algorithm/ATBD_DPR_201811_with_Appendix3b.pdf
- [19] R. Meneghini and T. Kozu, *Spaceborne Weather Radar*. Norwood, MA, USA: Artech House, 1990.
- [20] K. Kanamaru, T. Iguchi, T. Masaki, and T. Kubota, "Estimates of spaceborne precipitation radar pulsewidth and beamwidth using sea surface echo data," *IEEE Trans. Geosci. Remote Sens.*, vol. 58, no. 8, pp. 5291–5303, Aug. 2020, doi: [10.1109/TGRS.2019.2963090](https://doi.org/10.1109/TGRS.2019.2963090).
- [21] T. Kubota *et al.*, "Cloud assumption of precipitation retrieval algorithms for the dual-frequency precipitation radar," *J. Atmos. Ocean. Technol.*, vol. 37, no. 11, pp. 2015–2031, Nov. 2020.
- [22] D. W. Marquardt, "An algorithm for least-squares estimation of nonlinear parameters," *J. Soc. Ind. Appl. Math.*, vol. 11, no. 2, pp. 431–441, Jun. 1963.
- [23] T. T. Taylor, "Design of line-source antennas for narrow beamwidth and low side lobes," *Trans. IRE Prof. Group Antennas Propag.*, vol. 3, no. 1, pp. 16–28, Jan. 1955.
- [24] R. J. Mailloux, *Phased Array Antenna Handbook*, 3rd ed. Norwood, MA, USA: Artech House, 2017.
- [25] S. Seto, T. Iguchi, and T. Oki, "The basic performance of a precipitation retrieval algorithm for the global precipitation measurement Mission's single/dual-frequency radar measurements," *IEEE Trans. Geosci. Remote Sens.*, vol. 51, no. 12, pp. 5239–5251, Dec. 2013.
- [26] T. Iguchi, K. Kanamaru, and A. Hamada, "Possible improvement of the GPM's dual-frequency precipitation radar (DPR) algorithm," *Proc. SPIE*, vol. 10776, Sep. 2018, Art. no. 107760Q, doi: [10.1117/12.2324290](https://doi.org/10.1117/12.2324290).
- [27] *TRMM Precipitation Radar Team*. (2011). *Tropical Rainfall Measuring Mission (TRMM) Precipitation Radar Algorithm Instruction Manual For Version 7*. [Online]. Available: https://www.eorc.jaxa.jp/TRMM/documents/PR_algorithm_product_information/pr_manual/PR_Instruction_Manual_V7_L1.pdf
- [28] K. Kanamaru, T. Kubota, T. Iguchi, Y. N. Takayabu, and R. Oki, "Development of a precipitation climate record from spaceborne precipitation radar data—Part I: Mitigation of the effects of switching to redundancy electronics in the TRMM precipitation radar," *J. Atmos. Ocean. Technol.*, vol. 34, no. 9, pp. 2043–2057, Sep. 2017, doi: [10.1175/JTECH-D-17-0026.1](https://doi.org/10.1175/JTECH-D-17-0026.1).
- [29] N. Takahashi and T. Iguchi, "Estimation and correction of beam mismatch of the precipitation radar after an orbit boost of the tropical rainfall measuring mission satellite," *IEEE Trans. Geosci. Remote Sens.*, vol. 42, no. 11, pp. 2362–2369, Nov. 2004, doi: [10.1109/TGRS.2004.837334](https://doi.org/10.1109/TGRS.2004.837334).



Takeshi Masaki received the B.S. degree in science from Kochi University, Kochi, Japan, in 2006, and the M.S. degree in science from Kyoto University, Kyoto, Japan, in 2008.

Since 2009, he has been a Researcher with the Earth Environment Data Analysis and Research Group, Remote Sensing Technology Center of Japan, Tsukuba, Japan. His research interests are in calibration and algorithm development for spaceborne microwave radar for the Tropical Rainfall Measuring Mission (TRMM) and Global Precipitation Measurement (GPM) Mission.



Toshio Iguchi (Fellow, IEEE) received the B.Sc. degree from Hokkaido University, Sapporo, Japan, in 1976, the M.Sc. degree from the University of Tokyo, Tokyo, Japan, in 1978, and the Ph.D. degree from York University, Toronto, ON, Canada, in 1983.

Since 1985, he has been with the National Institute of Information and Communications Technology (formerly the Communications Research Laboratory), Koganei, Japan. He visited the NASA/Goddard Space Flight Center, Greenbelt,

MD, USA, from 1991 to 1994, performing the US–Japan collaborative experiment for measuring rain using airborne radar. Since then, he has focused primarily on issues related to the remote sensing of precipitation from space.



Kaya Kanemaru received the B.S. degree from Nagasaki University, Nagasaki, Japan, in 2009, and the M.S. and Ph.D. degrees from Nagoya University, Nagoya, Japan, in 2011 and 2014, respectively.

From 2014 to 2017, he was a Post-Doctoral Researcher with the Earth Observation Research Center, Japan Aerospace Exploration Agency, Tsukuba, Japan. From 2017 to 2019, he was a Project Researcher with the Atmosphere and Ocean Research Institute, University of Tokyo, Kashiwa, Japan. Since 2019, he has been a Researcher with the

Applied Electromagnetic Research Institute, National Institute of Information and Communications Technology, Koganei, Japan. His research interests include algorithm development and calibration for spaceborne microwave radar.

Dr. Kanemaru is a member of the Meteorological Society of Japan.



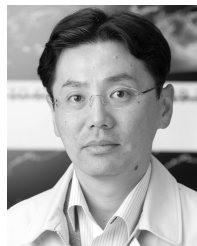
Kinji Furukawa received the B.S. and M.S. degrees in physics and geophysics from Tohoku University, Sendai, Japan, in 1988 and 1991, respectively.

In 1993, he joined the Japan Aerospace Exploration Agency (National Space Development Agency), Tokyo, Japan, where he was involved in the Tropical Rainfall Measuring Mission, the Global Precipitation Measurement Mission, and the Earth Clouds, Aerosols and Radiation Explorer Mission.



Naofumi Yoshida received the B.S. and M.S. degrees from Tohoku University, Sendai, Japan, in 1998 and 2000, respectively.

Since 2003, he has been with the Remote Sensing Technology Center of Japan, Tokyo, Japan. His interests are in low-level algorithm development and calibration for spaceborne microwave radar for the Tropical Rainfall Measuring Mission (TRMM) and Global Precipitation Measurement (GPM) Mission.



Takuji Kubota (Member, IEEE) received the B.S., M.S., and Ph.D. degrees in science from Kyoto University, Kyoto, Japan, in 1999, 2001, and 2004, respectively.

He was a Post-Doctoral Researcher with the Disaster Prevention Research Institute, Kyoto University, from 2004 to 2005, and with the Japanese Science Technology Agency, Tokyo, Japan, from 2005 to 2007. Since 2007, he has been a Researcher with the Earth Observation Research Center, Japan Aerospace Exploration Agency, Tsukuba, Japan. His

research interests are in algorithm development for spaceborne radar and microwave radiometers for the Tropical Rainfall Measuring Mission (TRMM), Global Precipitation Measurement (GPM) Mission, and EarthCARE Mission.

Dr. Kubota is a member of the Remote Sensing Society of Japan, Meteorological Society of Japan, Japan Geoscience Union, American Meteorological Society, and American Geophysical Union. He was a recipient of Prizes for Science and Technology in the Commendation for Science and Technology by the Minister of Education, Culture, Sports, Science and Technology in 2016 and the Gambo-Tatehira Award by the Meteorological Society of Japan in 2019.



Riko Oki received the Ph.D. degree in geophysics from The University of Tokyo, Tokyo, Japan, in 1995.

She joined the Remote Sensing Technology Center of Japan, Tokyo, in 1995. Since 1998, she has been with the National Space Development Agency of Japan (currently the Japan Aerospace Exploration Agency), Tokyo. She has been engaged in research on meteorology and climatology. She is a Chief Scientist with the Tropical Rainfall Measuring Mission/Global Precipitation Measurement Project

Group, Earth Observation Research Center, Japan Aerospace Exploration Agency, Tsukuba, Japan.